

# Regulating the Crystallization Kinetics and Lattice Strain of Lead-Free Perovskites with Perovskite Quantum Dots

Minchao Qin, Yuhao Li, Yingguo Yang, Pok Fung Chan, Shiang Li, Zhaotong Qin, Xuyun Guo, Lei Shu, Ye Zhu, Zhiyong Fan, Chun-Jen Su,\* and Xinhui Lu\*



Cite This: *ACS Energy Lett.* 2022, 7, 3251–3259



Read Online

ACCESS |



Metrics & More

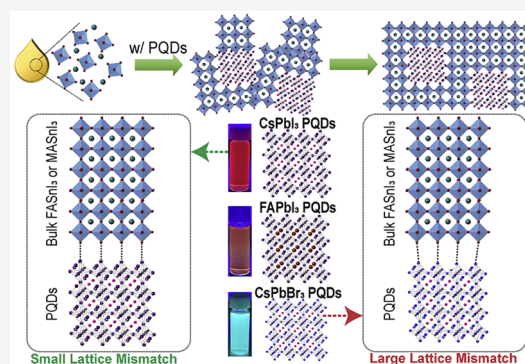


Article Recommendations



Supporting Information

**ABSTRACT:** The growth of high-quality tin-based perovskite films remains a grand challenge due to uncontrollable crystallization kinetics. Here, we report a facile strategy to realize an epitaxial-like growth of highly oriented tin-based perovskite films with the assistance of perovskite quantum dots (PQDs). Synchrotron-based in situ X-ray scattering results reveal that PQDs can act as nucleation centers to promote the growth of highly oriented perovskite crystals for both  $\text{FASnI}_3$  and  $\text{MASnI}_3$  systems. Remarkably, the degree of lattice strain can be readily modulated by tuning the lattice mismatch between various PQDs and bulk perovskites, thus reducing defect density and improving efficiencies. The efficiency of  $\text{MASnI}_3$  PSCs with PQDs has been pushed to 12.49%, which is the highest of this type reported so far. Furthermore, the film and device stability are enhanced owing to the improved film quality and the protection of hydrophobic ligands from PQDs.



Lead halide perovskites have demonstrated great potential in the photovoltaic field, while the toxicity of lead becomes one of the major obstacles on the road to their commercialization.<sup>1</sup> Alternatively, environmentally friendly perovskites based on nontoxic tin ions ( $\text{Sn}^{2+}$ ), possessing a similar outer electronic structure and ionic radius with lead ions ( $\text{Pb}^{2+}$ ),<sup>2</sup> have attracted increasing research efforts, giving rise to rapidly rising power conversion efficiencies (PCEs) in recent years.<sup>3</sup> Contrary to Pb-based perovskites, Sn-based perovskites exhibit a smaller band gap (1.3–1.4 eV), which is closer to the optimal value to reach the theoretical maximum efficiency of 33% under the Shockley–Queisser limit.<sup>4</sup> However, currently reported PCEs of Sn-based perovskite solar cells (PSCs) still lag far behind those of Pb-based PSCs.<sup>5</sup>

At the current stage, the poor film quality of Sn-based PSCs is one critical reason for the worse device performance than Pb-based PSCs. It was mainly attributed to the uncontrollable crystallization due to the higher reactivity of Lewis acidity of  $\text{SnI}_2$ .<sup>6</sup> The random crystal growth will lead to poor crystallinity,<sup>7</sup> disordered crystals,<sup>8</sup> high defect density,<sup>9</sup> and pinholes.<sup>10</sup> Many efforts have been devoted to modulating the crystallization process of Sn-based perovskites by means of incorporating Lewis base additives,<sup>6</sup> ionic liquid,<sup>11</sup> long-chain ammonium cations,<sup>12</sup> etc. Regulating the perovskite growth

with templates is another effective approach to depositing high-quality perovskite films, which has been widely reported in Pb-based perovskites.<sup>13</sup> For instance, Bi et al. used poly(methyl methacrylate) (PMMA) as a template to control  $\text{FAPbI}_3$ -based perovskite crystal nucleation and growth, achieving shiny smooth perovskite films with excellent electronic properties.<sup>14</sup> Zhang et al. reported a template-guided growth of  $\alpha$ - $\text{FAPbI}_3$  perovskites based on a BA-related intermediate phase and achieved increased film crystallinity and reduced defects.<sup>15</sup> Although templates can serve as nucleation centers for the perovskite growth, a large lattice mismatch between the templating materials and perovskites may induce severe lattice strain, thereby undermining the device performance.<sup>16</sup> An ideal templating material for the perovskite crystal growth could be the perovskite crystal itself,<sup>17</sup> but a bottom perovskite templating layer can be entirely dissolved by dimethylformamide (DMF) or dimethyl

Received: July 26, 2022

Accepted: September 1, 2022

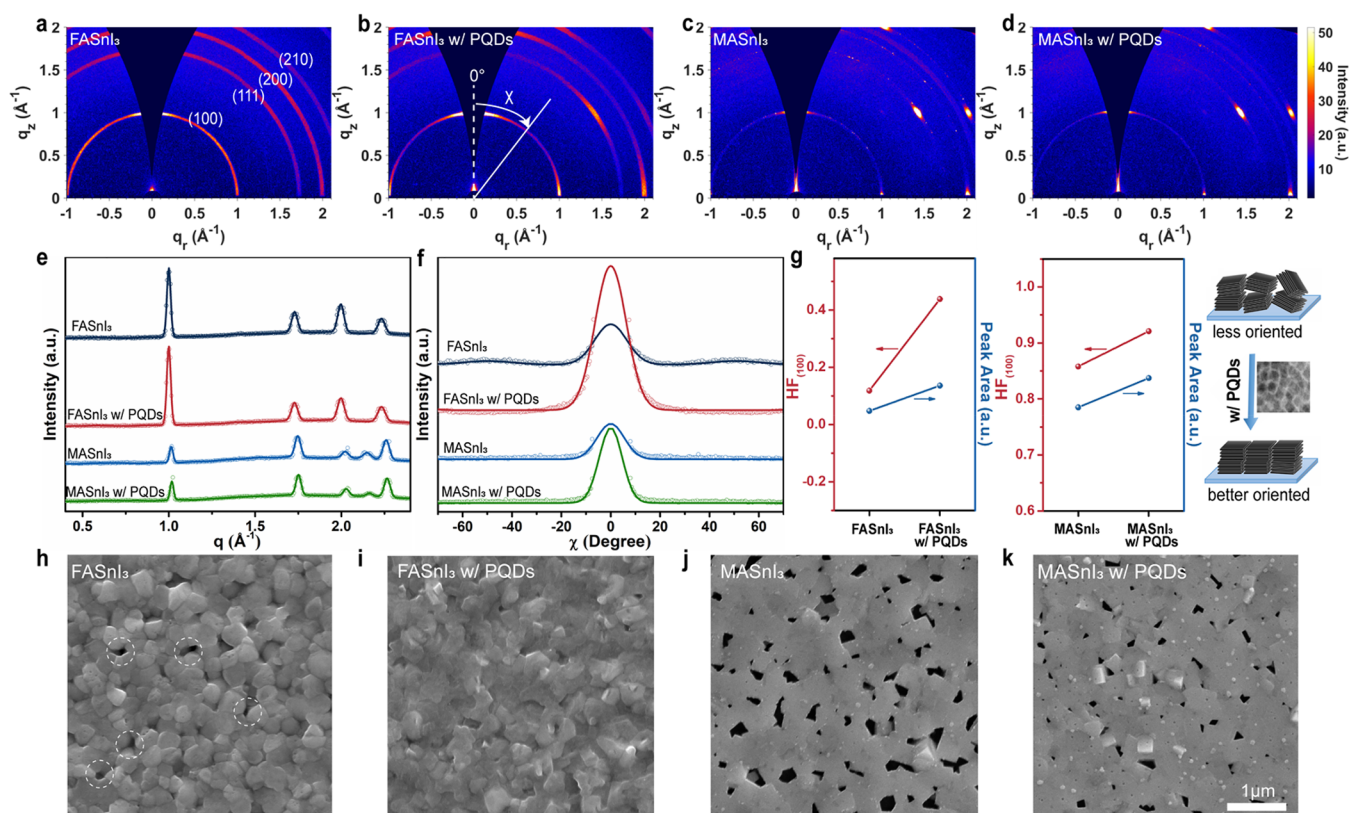


**Figure 1.** GIWAXS patterns of (a) FASnI<sub>3</sub>, (b) FASnI<sub>3</sub> with PQDs, (c) MASnI<sub>3</sub>, and (d) MASnI<sub>3</sub> with PQDs. Corresponding GIWAXS (e) sector intensity profiles and (f) polar intensity profiles along the (100) ring in the  $q$  range of 0.95–1.05 Å<sup>-1</sup>. (g) Calculated Hermans' orientation factor (HF) and fitted peak areas referring to (100) peaks for FASnI<sub>3</sub> and MASnI<sub>3</sub> perovskites, and schematics of the orientation change of perovskite (100) planes. SEM images of perovskite films based on (h) FASnI<sub>3</sub>, (i) FASnI<sub>3</sub> with PQDs, (j) MASnI<sub>3</sub>, and (k) MASnI<sub>3</sub> with PQDs.

sulfoxide (DMSO) solvents from the perovskite precursor. Therefore, a judicious selection of perovskite templating materials could potentially improve the film quality of Sn-based perovskite film, therefore worthwhile to explore.

Herein, perovskite quantum dots (PQDs) were adopted as the templating materials to assist the highly oriented crystal growth of bulk tin halide perovskite films. The capping ligands of PQDs can protect themselves from being dissolved by precursor solvents, and, at the same time, the single-crystal interior of PQDs can serve as the nucleation centers for an epitaxial-like growth of tin halide perovskite crystallites. Consequently, the incorporation of only a trace amount of PQDs in FASnI<sub>3</sub> films can largely enhance the orientation order and accelerate the crystallization process with the aid of PQD nucleation sites, as revealed by in situ grazing-incidence wide-angle X-ray scattering (GIWAXS) measurements. Furthermore, the lattice strain can be readily modulated by tuning the lattice mismatch between bulk tin perovskites and PQDs. Two bulk tin perovskite systems and three PQDs are combined mutually to finetune the degree of lattice mismatch. The combinations with a smaller lattice mismatch and released lattice strain exhibit reduced defect density and improved device performance. The FASnI<sub>3</sub>-based PSCs have achieved benchmark PCEs of over 13% with this strategy. The efficiency of MASnI<sub>3</sub>-based PSCs with PQDs has been boosted to 12.49%, which is the highest reported efficiency of this type to date. Furthermore, the film and device stability have also been considerably enhanced, which are attributed to the improved film quality and the humidity and oxidation protection from

the hydrophobic ligands on PQDs. This work suggests a generally applicable way to grow high-quality tin halide perovskite films by introducing PQDs with matching lattice constants, paving the way to the real application of environmentally friendly perovskite optoelectronic devices.

## ■ MICROSTRUCTURES OF TIN HALIDE PEROVSKITE FILMS WITH PQDS

Tin halide perovskite films were deposited through a one-step antisolvent spin-coating process (Supporting Information Figure S1), and CsPbI<sub>3</sub> PQDs were incorporated into tin halide perovskite films by dripping PQD-contained chlorobenzene (0.5 mg/mL) as the antisolvent during the spinning process. The CsPbI<sub>3</sub> PQDs with an average size of around 9 nm were synthesized via a conventional hot injection method,<sup>18</sup> as demonstrated by TEM, photoluminescence (PL), and XRD spectra in Figure S2. It is noted that only a trace amount of CsPbI<sub>3</sub> PQDs are incorporated in the FASnI<sub>3</sub> film in light of XPS results that the Pb/Sn ratio in the final FASnI<sub>3</sub> films with PQDs is estimated to be around 0.12% (Figure S3). After incorporating PQDs in FASnI<sub>3</sub> perovskite films, the peak intensities of (100) and (200) peaks in XRD spectra (Figure S4) are drastically enhanced, which may come from the change of crystal orientation. Therefore, two-dimensional (2D) GIWAXS measurements were conducted to further investigate the microstructures of FASnI<sub>3</sub> perovskite films without and with PQDs, as shown in Figure 1a,b. The corresponding sector intensity profiles and polar intensity profiles along the (100) ring at ( $\sim$ 0.99 Å<sup>-1</sup>) are presented in

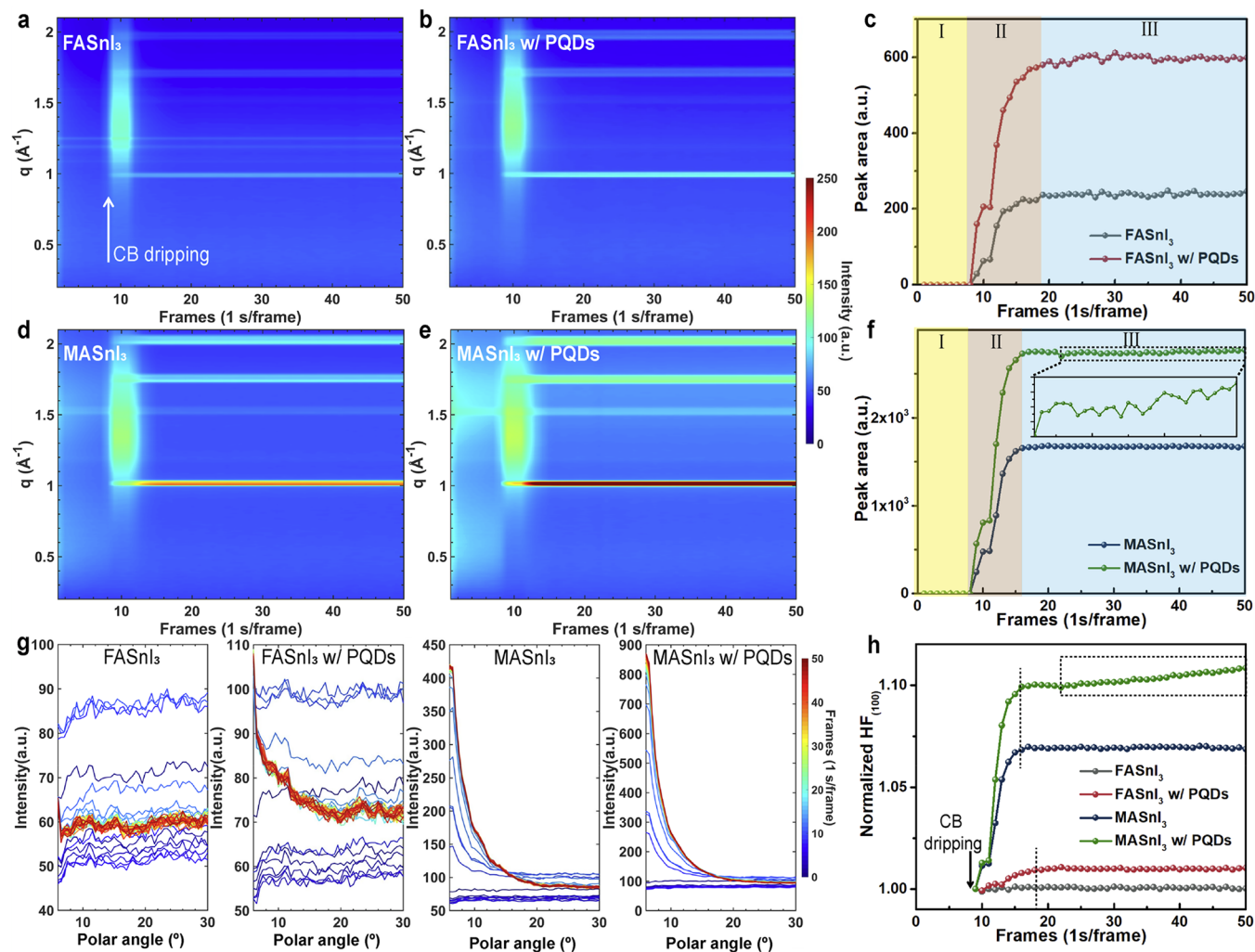


**Figure 2.** Time-resolved GIWAXS profile analysis during the spin-coating process. False-color intensity maps versus wavenumber  $q$  and frame numbers for FASnI<sub>3</sub> films (a) without and (b) with PQDs. (c) Corresponding time evolutions of FASnI<sub>3</sub> (100) peak areas. False-color intensity maps for MASnI<sub>3</sub> films (d) without and (e) with PQDs. (f) Corresponding time evolutions of MASnI<sub>3</sub> (100) peak areas. (g) Time-resolved polar intensity profiles for the (100) peaks of FASnI<sub>3</sub>, FASnI<sub>3</sub> with PQDs, MASnI<sub>3</sub>, and MASnI<sub>3</sub> with PQDs. (h) Real-time changes of normalized HF<sub>(100)</sub> during spin-coating.

Figure 1e,f, respectively. Compared with the neat FASnI<sub>3</sub> film, the film with PQDs exhibits better crystallinity considering the larger peak area. The film with PQDs also shows a preferred crystal orientation with the (100) planes parallel to the substrate. To study the crystallite orientational order quantitatively, Hermans' orientation factor (HF)<sup>19,20</sup> was calculated based on the polar intensity profiles along the (100) ring in the  $q$  range of 0.95–1.05 Å<sup>-1</sup> in Figure 1g and the detailed calculation scheme is included in the Supplementary Information Note S1. With the incorporation of PQDs, the HF value increases from 0.12 to 0.44, which suggests that the out-of-plane orientational order of the (100) planes of FASnI<sub>3</sub> perovskites was greatly enhanced, being beneficial to the exciton diffusion and charge transport in the films.<sup>21</sup> A similar trend was observed in the MASnI<sub>3</sub> system, as demonstrated in Figure 1c,d,g. Although the neat MASnI<sub>3</sub> perovskite film already shows a highly ordered crystal orientation, the incorporation of PQDs can further improve the HF from 0.86 to 0.92 as well as the diffraction peak area demonstrating a higher crystallinity (Figure 1g). It is noted that the (100) peak position of MASnI<sub>3</sub> perovskites shifts to

~1.01 Å<sup>-1</sup> compared with the peak position of FASnI<sub>3</sub> perovskites (~0.99 Å<sup>-1</sup>) owing to the relatively smaller ionic radius of MA<sup>+</sup> than FA<sup>+</sup>.

The film morphology of tin halide perovskites was also improved with PQDs, as demonstrated by the scanning electron microscopy (SEM) images in Figure 1h–k. PQDs can eliminate pinholes in FASnI<sub>3</sub> films, and it is more prominent in MASnI<sub>3</sub> films that the number and size of pinholes are significantly reduced after introducing PQDs (Figure 1k). In brief, the incorporation of PQDs in both FASnI<sub>3</sub> and MASnI<sub>3</sub> systems can simultaneously improve the film morphology, increase film crystallinity, and enhance the crystal orientation, all of which may originate from the distinct crystallization kinetics with the assistance of PQDs as discussed in the following.<sup>22</sup>

## CRYSTALLIZATION KINETICS OF TIN HALIDE PEROVSKITES WITH PQDS

To understand the PQD-assisted tin halide perovskite crystallization mechanism, in situ GIWAXS measurements were carried out to monitor the real-time film formation

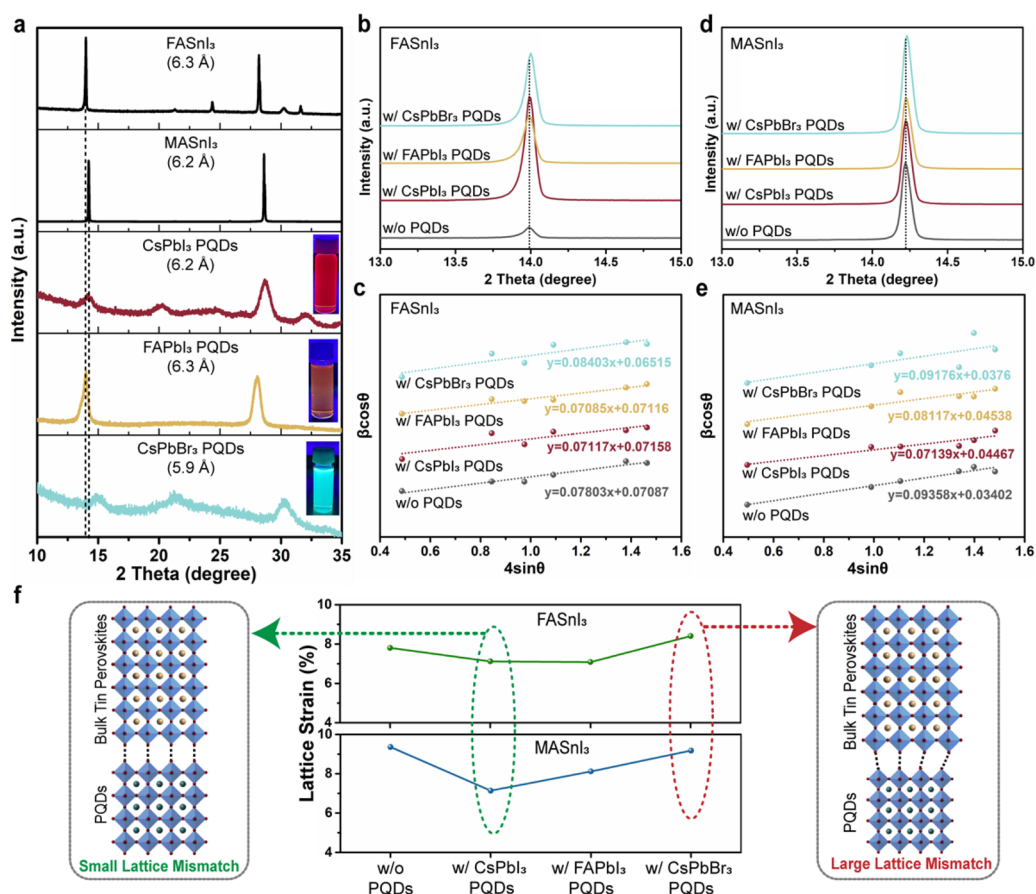


**Figure 3.** (a) XRD spectra of the neat FASnI<sub>3</sub> film, neat MASnI<sub>3</sub> film, pure CsPbI<sub>3</sub> PQD film, pure FAPbI<sub>3</sub> PQD film, and pure CsPbBr<sub>3</sub> PQD film. (b) XRD spectra, and (c) Williamson–Hall plots (data are displaced for clarity) for the FASnI<sub>3</sub> films without and with different PQDs. (d) XRD spectra, and (e) Williamson–Hall plots (data are displaced for clarity) for the MASnI<sub>3</sub> films without and with different PQDs. (f) Summary of estimated lattice strains in FASnI<sub>3</sub> and MASnI<sub>3</sub> films without and with different PQDs, and schematic illustrations of the relationships between the lattice strain and lattice mismatch.

process during spin-coating (Figure 2).<sup>23,24</sup> The antisolvent chlorobenzene without or with PQDs was dripped at the 9th second, as manifested by the broad peak centered at  $\sim 1.35 \text{ \AA}^{-1}$  (Figure S5). The antisolvent dripping ended the perovskite precursor stage I and triggered the crystallization of the tin halide perovskite phase (stage II). It is worth mentioning that, unlike Pb-based perovskites,<sup>25,26</sup> the perovskite phase was directly formed in both FASnI<sub>3</sub> (Figure 2a) and MASnI<sub>3</sub> (Figure 2d) systems without experiencing any intermediate phases or hexagonal yellow phases, due to the lower formation energy of tin halide perovskites.<sup>27</sup> The incorporation of PQDs in FASnI<sub>3</sub> perovskites plays an important role in promoting perovskite nucleation and crystal growth during stage II, leading to an accelerated crystallization process (Figure 2c). The crystal growth ended at around the 18th second and the FASnI<sub>3</sub> film with PQDs remained at higher crystallinity during stage III. The same phenomenon was also observed in MASnI<sub>3</sub> perovskites. The (100) peak area of the MASnI<sub>3</sub> film with PQDs grew much more rapidly than that of the neat MASnI<sub>3</sub> film during stage II (Figure 2f), indicative of much faster crystallization kinetics with PQDs. It is noted that the MASnI<sub>3</sub> film with PQDs still experienced a slow crystal growth during stage III, which could be one of the possible reasons for the mitigated pinholes among the film (Figure 1k).

Interestingly, in addition to the crystal growth rate, the orientational order of FASnI<sub>3</sub> and MASnI<sub>3</sub> films also gradually

increases during the film-formation process, which is rarely observed, as in most cases, the orientational order remains the same or even decreases during perovskite crystal growth.<sup>28</sup> Figure 2g presents time-resolved polar intensity profiles for the perovskite (100) peaks with the corresponding evolution of normalized HF<sub>(100)</sub> summarized in Figure 2h. We found that the orientational order of FASnI<sub>3</sub> perovskites nearly remained unchanged during the crystallization process, while progressive enhancement of HF<sub>(100)</sub> was observed after incorporating PQDs during stage II. It suggests that PQDs will intensify the crystal orientational order of FASnI<sub>3</sub> perovskites during the crystal nucleation and growth stage. As for MASnI<sub>3</sub> perovskites, the value of HF<sub>(100)</sub> was increased during stage II regardless of the assistance of PQDs, indicating that neat MASnI<sub>3</sub> perovskite films already possess a preferred crystal orientation, which is consistent with ex situ GIWAXS results in Figure 1c and previous reports.<sup>29</sup> Nonetheless, the crystal orientation of MASnI<sub>3</sub> perovskites was reinforced after introducing PQDs owing to the higher HF<sub>(100)</sub> during stage II and further increasing HF<sub>(100)</sub> during stage III (Figure 2h).

Considering that the native iodide vacancies and the partially exposed Pb–I octahedra at the PQD surface matrix could induce the crystal nucleation,<sup>30,31</sup> we postulate that the highly ordered Pb–I octahedra in PQDs, with small lattice mismatches (CsPbI<sub>3</sub> PQDs 6.2 Å vs FASnI<sub>3</sub> 6.3 Å vs MASnI<sub>3</sub> 6.2 Å), can serve as crystal nuclei and activate an

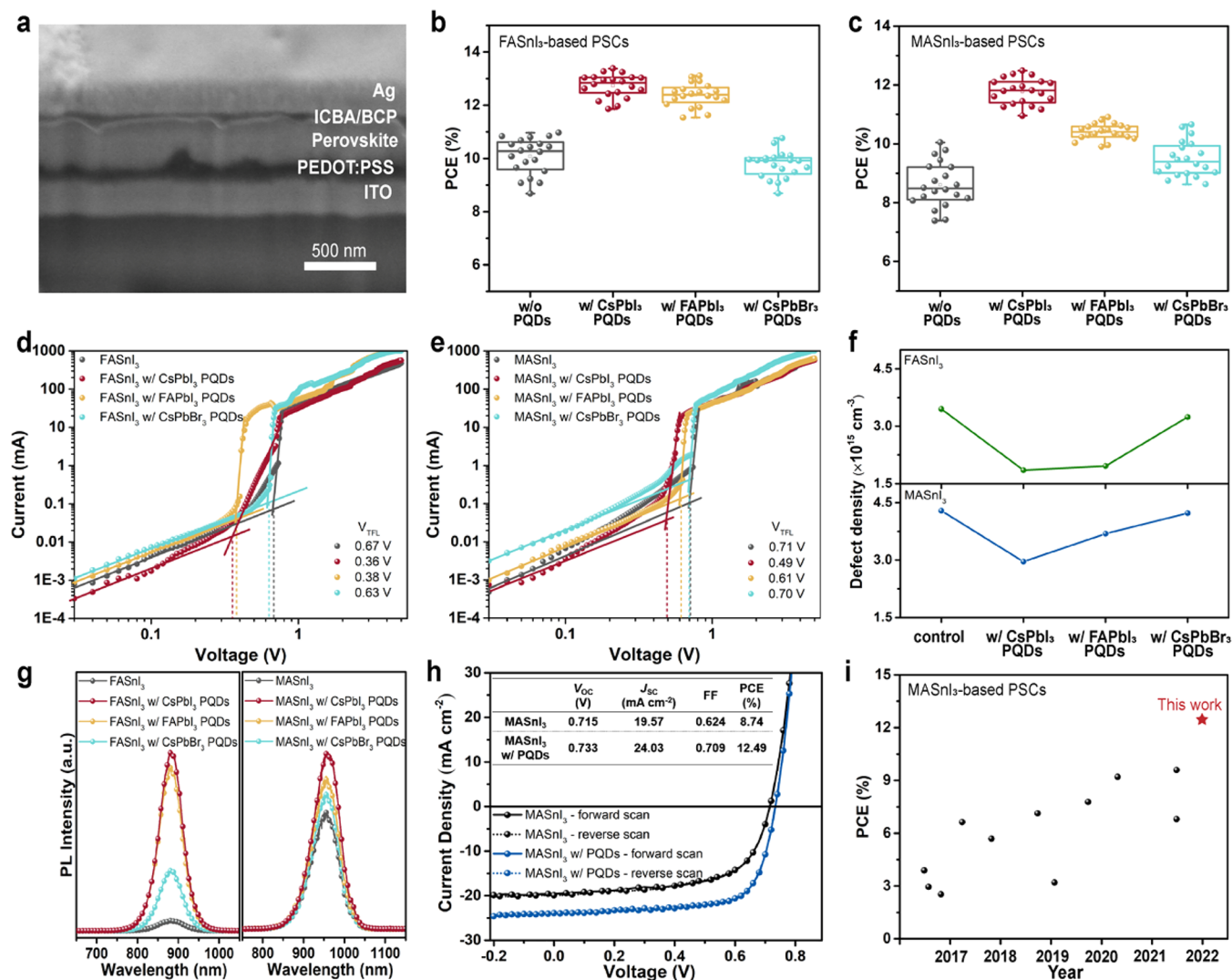


**Figure 4.** (a) Cross-sectional SEM image of a whole device with the structure of ITO/PEDOT:PSS/perovskite/ICBA/BCP/Ag. Device efficiency statistics of PSCs based on (b) FASnI<sub>3</sub> and (c) MASnI<sub>3</sub> films without and with different PQDs. Dark current–voltage measurements of the electron-only devices based on (d) FASnI<sub>3</sub> films and (e) MASnI<sub>3</sub> films, and (f) corresponding estimated defect densities. (g) PL spectra of FASnI<sub>3</sub> and MASnI<sub>3</sub> films without and with different PQDs. (h)  $J$ – $V$  curves of the PSCs based on MASnI<sub>3</sub> films without and with PQDs. (i) Progress of efficiency of PSCs based on MASnI<sub>3</sub> perovskites.

epitaxial-like growth for oriented tin halide perovskite crystallites, as illustrated in Figure S6. The incorporation of PQDs can promote the crystal nucleation and growth as nucleation sites, and the epitaxial-like growth based on the highly ordered Pb–I octahedra in PQDs can give rise to tin halide perovskite films with a preferred crystal orientation and high crystallinity.

In order to further demonstrate the role of PQDs as nucleation centers in the growth of tin halide perovskites, we carried out a series of comparative experiments by adding separate components from PQDs to determine whether it is the decomposed components or the whole piece of PQDs that are critically affecting the perovskite crystal growth. First, the ligands of PQD—pure oleic acid (OA) and oleylamine (OAm)—were added to chlorobenzene and incorporated into FASnI<sub>3</sub> perovskite films through the same antisolvent fabrication procedure. It is found that only OA or OAm ligands cannot induce the formation of vertically oriented FASnI<sub>3</sub> crystallites according to the almost unchanged peak intensity ratio between the (100) plane and other planes (e.g., (111)

plane) (Figure S7). It is likely because the carbon chain lengths of OA and OAm ligands are too long to form an ordered crystal structure.<sup>32</sup> Second, different concentrations of CsI and PbI<sub>2</sub> with the molar ratio of 1:1 were incorporated into FASnI<sub>3</sub> films to investigate the consequences of element doping of Cs<sup>+</sup> and Pb<sup>2+</sup>. Likewise, the crystal orientation in FASnI<sub>3</sub> films is basically unchanged regardless of the concentrations of CsI and PbI<sub>2</sub> (Figure S8), indicating that the change in crystal orientation is not caused by the element doping either. Nevertheless, a high concentration of CsI in FASnI<sub>3</sub> perovskites will induce the XRD peak shift to a larger  $2\theta$  region due to the shrinkage of the crystal lattice with smaller Cs<sup>+</sup>. In contrast, the incorporation of CsPbI<sub>3</sub> PQDs, even at a high concentration, does not lead to the peak shift but only the peak intensity increases in XRD spectra, as shown in Figure S9. It implies that the PQDs will not be decomposed into individual elements and doped into the perovskite crystal lattice. As the concentration of PQDs increased, we found that both perovskite peak intensity and HF values were gradually enhanced (Figure S9c), further confirming that the incorpo-

ration of PQDs will lead to a predominantly vertically oriented perovskite crystallites in films. It is noted that the PQDs are uniformly distributed throughout the whole depth of the film (Figure S10). Besides, we also synthesized CsPbI<sub>3</sub> PQDs with different sizes (i.e., 6 and 12 nm), as shown in Figure S11, and found that the incorporation of CsPbI<sub>3</sub> PQDs with different sizes can also give rise to enhanced and similar crystal orientation (Figure S12).

### ■ LATTICE STRAIN MODULATION VIA DIFFERENT PQDS AS NUCLEATION CENTERS

The lattice mismatch between the template and the crystal grown on top critically affects the final film quality such as the lattice strain in the film.<sup>33,34</sup> Therefore, we first investigated the growth of 3D FASnI<sub>3</sub> on three different PQDs (CsPbI<sub>3</sub>, FAPbI<sub>3</sub>, and CsPbBr<sub>3</sub>) with different lattice constants (Figure 3a and Figure S13), to confirm the hypothesis of PQD-templated epitaxial-like growth of perovskite film. We found that the (100) peak of the FASnI<sub>3</sub> film with CsPbBr<sub>3</sub> PQDs exhibits a peak shift to a higher  $2\theta$  region, as shown in Figure 3b, indicative of a lattice contraction with CsPbBr<sub>3</sub> PQDs. Since it has been demonstrated that PQDs are not incorporated into FASnI<sub>3</sub> crystal lattices as element doping (Figures S8 and S9), the lattice contraction in the FASnI<sub>3</sub> film with CsPbBr<sub>3</sub> PQDs should arise from the lattice strain which is induced by relatively larger lattice mismatch (6.8%). The Williamson–Hall method was then employed to estimate the lattice strain in the FASnI<sub>3</sub> films,<sup>24,35</sup> as shown in Figure 3c. It is found that the lattice strain is relaxed after incorporating CsPbI<sub>3</sub> and FAPbI<sub>3</sub> PQDs (Figure 3f), which may be due to the better crystal orientation and a negligible lattice mismatch between bulk FASnI<sub>3</sub> and FAPbI<sub>3</sub>/CsPbI<sub>3</sub> PQDs.<sup>36,37</sup> It is noted that the CsPbI<sub>3</sub> PQDs with different sizes can also relax the lattice strain in the FASnI<sub>3</sub> perovskite film (Figure S14) due to the unchanged lattice constant of PQDs (Figure S11f). On the contrary, the FASnI<sub>3</sub> perovskite films with CsPbBr<sub>3</sub> PQDs exhibit higher lattice strain with a relatively larger lattice mismatch, which well explains the reason for the lattice contraction in the film.<sup>34</sup> Remarkably, the incorporation of all of these PQDs can lead to a drastic increase in peak intensities in XRD spectra (Figure S15) and better crystal orientation based on the GIWAXS results (Figure S16), further confirming the roles of PQDs in the oriented growth of bulk tin halide perovskites.

To study the generality of PQD-assisted perovskite crystal growth and the effects of lattice mismatch on the lattice strain in the film, MASnI<sub>3</sub>, possessing a slightly smaller lattice constant of 6.2 Å than that of FASnI<sub>3</sub> (6.3 Å), was also studied with three different PQDs. The (100) peak of the MASnI<sub>3</sub> film with CsPbBr<sub>3</sub> PQDs also shifted to a larger diffraction angle (Figure 3d), corresponding to a lattice contraction, as observed in the FASnI<sub>3</sub> film. In the meantime, according to the Williamson–Hall plots in Figure 3e, it exhibits an increased lattice strain compared with the FA-based counterpart, due to a larger lattice mismatch between the PQD and 3D perovskites. Furthermore, the lattice strain is significantly released in the MASnI<sub>3</sub> film with CsPbI<sub>3</sub> PQDs, owing to their perfectly matched lattice constants of 6.2 Å. It is evident that the lattice strain can be modulated by a judicious selection of bulk tin halide perovskites and PQD nucleation centers, based on different lattice constants. As demonstrated in Figure 3f, a small lattice mismatch between PQD templates and tin halide

perovskites can relax the lattice strain, whereas a large lattice mismatch will increase the lattice strain.

### ■ ENHANCED DEVICE PERFORMANCE AND STABILITY OF PSCS WITH PQDS

We then investigated the influence of incorporating different types of PQDs on both FASnI<sub>3</sub> and MASnI<sub>3</sub>-based device performance (Figure 4a). The device efficiency statistics of PSCs based on FASnI<sub>3</sub> and MASnI<sub>3</sub> films are presented in Figures 4b, S17 and Figures 4c, S18, respectively. Overall, for the FASnI<sub>3</sub> system, the PSCs with CsPbI<sub>3</sub> PQDs and FAPbI<sub>3</sub> PQDs exhibit comparable PCEs, both exceeding 13%, which are much higher than those of PSCs without PQDs. The PCE increase is mainly attributed to the increased open-circuit voltage ( $V_{OC}$ ) and fill factor (FF). In contrast, the device efficiency decreases after incorporating CsPbBr<sub>3</sub> PQDs because of the poor short-circuit current density ( $J_{SC}$ ) and FF. Interestingly, the FASnI<sub>3</sub> device efficiency increases (Figure 4b) in accordance with the release of lattice strain (Figure 3f). A similar trend was observed in the MASnI<sub>3</sub> system (Figure 4c). It is known that the lattice strain in the crystal is responsible for defect formation.<sup>34</sup> To examine the defect density in the perovskite films without and with PQDs, we conducted space-charge-limited current (SCLC) measurements for both FASnI<sub>3</sub> and MASnI<sub>3</sub> perovskite films (Figure 4d,e), with the calculated defect densities ( $N_t$ ) summarized in Figure 4f. Remarkably, for both FASnI<sub>3</sub> and the MASnI<sub>3</sub> systems, the films with CsPbI<sub>3</sub> PQDs exhibit relatively lower defect densities than the films with CsPbBr<sub>3</sub> PQDs which is correlated with the smaller lattice strains (Figure 3f) from the mitigated lattice mismatch between CsPbI<sub>3</sub> PQDs and the two 3D Sn-based perovskite systems. Steady-state PL spectra in Figure 4g also reveal the largely enhanced PL intensities for the films with CsPbI<sub>3</sub> PQDs, indicating the reduction of nonradiative recombination as a result of lower defect density. Note that the PL peak positions of FASnI<sub>3</sub> and MASnI<sub>3</sub> films are 882 nm ( $\sim 1.4$  eV) and 958 nm ( $\sim 1.3$  eV), respectively.

MASnI<sub>3</sub>-based PSCs usually exhibit lower efficiencies than FASnI<sub>3</sub>-based PSCs.<sup>38</sup> In addition, it is reported that the formation energy of Sn vacancies in MASnI<sub>3</sub> perovskite films is lower than that in FASnI<sub>3</sub> due to the stronger antibonding coupling between Sn 5s and I 5p, resulting in higher defect density.<sup>27</sup> We indeed found that MASnI<sub>3</sub> perovskite films have relatively higher defect densities and more pinholes than the FASnI<sub>3</sub> perovskite films. Nonetheless, the incorporation of PQDs in MASnI<sub>3</sub> perovskite films can dramatically suppress the formation of pinholes (Figure 1k) and reduce the defect density (Figure 4f). As a result of the considerably improved film quality of MASnI<sub>3</sub> films with PQDs, the device efficiency of MASnI<sub>3</sub>-based PSCs is significantly boosted from 8.74 to 12.49% with negligible hysteresis (Figure 4h), which is the highest PCE reported among the MASnI<sub>3</sub> PSCs so far (Figure 4i and Table S1).<sup>39–41</sup> The  $J_{SC}$  values are confirmed by the external quantum efficiency (EQE) measurements in Figure S19.

The poor stability of tin halide perovskites in ambient air has been a serious issue mainly due to the oxidation of Sn<sup>2+</sup> to Sn<sup>4+</sup>. In the meantime, the involvement of moisture in ambient air will establish a cyclic degradation pathway,<sup>42</sup> thus largely accelerating the oxidation and degradation of tin halide perovskites. Therefore, preventing Sn-based perovskite films from the penetration of moisture is a crucial means to hinder the oxidation. Here, the OA and OAm ligands from PQDs are

hydrophobic, so the incorporation of PQDs largely alters the surface wettability of perovskite film. The water contact angle increases considerably from  $47.5^\circ$  to  $80.0^\circ$  (Figure S22a). The O 1s signal from ligands in XPS spectra (Figure S20) also indicates the existence of ligands on the film surface. As a consequence, the degradation of Sn-based perovskites with PQDs has been considerably slowed compared with the film without PQDs during the storage in ambient air, as manifested by the formation of vacancy-ordered double perovskites<sup>42</sup> in XRD spectra in Figure S21. Furthermore, XPS measurements reveal that the content of Sn(IV) in fresh perovskite films is reduced from 7.4% to 1.8% with the incorporation of PQDs (Figure S22b). After storage in ambient for  $\sim 3$  h, the content of oxidized Sn(IV) in the film without PQDs significantly increases to 83.8% while the film with PQDs retains relatively less Sn(IV) content of 40.0% (Figure S22b,c). It suggests that PQDs can largely suppress the oxidation of Sn(II) to Sn(IV) in tin halide perovskite films, thus contributing to the superior photovoltaic performance as well as stability. The structural stability of the FASnI<sub>3</sub> films with PQDs under 1 sun continuous illumination was explored by virtue of time-resolved in situ GIWAXS measurements. As presented in Figure S22d, e, the (100) peak intensity only experiences a tiny drop, indicative of the good structural stability of FASnI<sub>3</sub> films with PQDs under light stress. In addition, both unencapsulated FASnI<sub>3</sub> and MASnI<sub>3</sub> PSCs with PQDs exhibit better stability under dark condition (Figure S22f) and continuous light illumination (Figure S22g) than control samples without PQDs.

In summary, we employed PQDs as templates to induce the quasi-epitaxial growth of high-quality tin halide perovskite films. A trace amount of PQDs, serving as nucleation sites, not only enhances the crystal orientation order of tin halide perovskites but also promotes the formation of the perovskite phase by accelerating the crystallization kinetics. Remarkably, the lattice strain among both FASnI<sub>3</sub> and MASnI<sub>3</sub> perovskite films can be fine-tuned by choosing different PQD templates (i.e., CsPbI<sub>3</sub>, CsPbBr<sub>3</sub>, and FAPbI<sub>3</sub> PQDs) with different lattice constants. The lattice strain in tin halide perovskite films is relaxed with the aid of CsPbI<sub>3</sub> PQDs owing to the minor lattice mismatch, thus diminishing the defect density and enhancing device performance for both FASnI<sub>3</sub> and MASnI<sub>3</sub> systems. It is worth noting that MASnI<sub>3</sub>-based PSCs have been reported to suffer from poor film morphology, high defect densities, and thus much worse device performance than the FASnI<sub>3</sub> counterparts.<sup>27,43</sup> The incorporation of PQDs can significantly improve the MASnI<sub>3</sub> film morphology and suppress the formation of defects, giving rise to a record efficiency of 12.49% for MASnI<sub>3</sub>-based PSCs. Moreover, improved structural stability under moisture and light stresses was also observed, which is attributed to the protection of hydrophobic ligands from PQDs. We believe that PQD-assisted growth of high-quality perovskites is a universal strategy applicable in various perovskite systems, as previous studies on Pb-based perovskite light-emitting diodes and solar cells also reported that PQDs can act as nucleation sites<sup>44,45</sup> and surface passivation agents.<sup>46,47</sup> Further explorations of a variety of PQDs (e.g., MAPbI<sub>3</sub> PQDs, CsSnI<sub>3</sub> PQDs, and FASnI<sub>3</sub> PQDs) in different bulk perovskite systems with tunable lattice strain could be of great interest in the field.

## ■ ASSOCIATED CONTENT

### Supporting Information

The Supporting Information is available free of charge at <https://pubs.acs.org/doi/10.1021/acseenergylett.2c01692>.

Supplementary notes; experimental section; film fabrication schematics; TEM images; PL, XRD, XPS, and EQE spectra; GIWAXS intensity profiles and additional patterns; EDX maps; ToF-SIMS depth profiles; Williamson–Hall plots; device performance statistics (PDF)

## ■ AUTHOR INFORMATION

### Corresponding Authors

Xinhui Lu – Department of Physics, The Chinese University of Hong Kong, 999077 Hong Kong SAR, China; [orcid.org/0000-0002-1908-3294](https://orcid.org/0000-0002-1908-3294); Email: [xinhui.lu@cuhk.edu.hk](mailto:xinhui.lu@cuhk.edu.hk)

Chun-Jen Su – National Synchrotron Radiation Research Center, Hsinchu Science Park, Hsinchu 30076, Taiwan; Email: [su.cj@nsrrc.org.tw](mailto:su.cj@nsrrc.org.tw)

### Authors

Minchao Qin – Department of Physics, The Chinese University of Hong Kong, 999077 Hong Kong SAR, China; [orcid.org/0000-0001-8819-2307](https://orcid.org/0000-0001-8819-2307)

Yuhao Li – Department of Physics, The Chinese University of Hong Kong, 999077 Hong Kong SAR, China

Yingguo Yang – Shanghai Synchrotron Radiation Facility (SSRF), Shanghai Advanced Research Institute & Chinese Academy of Sciences, Shanghai 201204, China; [orcid.org/0000-0002-1749-2799](https://orcid.org/0000-0002-1749-2799)

Pok Fung Chan – Department of Physics, The Chinese University of Hong Kong, 999077 Hong Kong SAR, China

Shiang Li – Department of Physics, The Chinese University of Hong Kong, 999077 Hong Kong SAR, China

Zhaotong Qin – Department of Physics, The Chinese University of Hong Kong, 999077 Hong Kong SAR, China

Xuyun Guo – Department of Applied Physics, Research Institute for Smart Energy, The Hong Kong Polytechnic University, 999077 Hong Kong SAR, China; [orcid.org/0000-0003-0365-7545](https://orcid.org/0000-0003-0365-7545)

Lei Shu – Department of Electronic and Computer Engineering, The Hong Kong University of Science and Technology, 999077 Hong Kong SAR, China

Ye Zhu – Department of Applied Physics, Research Institute for Smart Energy, The Hong Kong Polytechnic University, 999077 Hong Kong SAR, China

Zhiyong Fan – Department of Electronic and Computer Engineering, The Hong Kong University of Science and Technology, 999077 Hong Kong SAR, China; [orcid.org/0000-0002-5397-0129](https://orcid.org/0000-0002-5397-0129)

Complete contact information is available at: <https://pubs.acs.org/10.1021/acseenergylett.2c01692>

### Author Contributions

X.L. supervised the work. M.Q. and Y.L. contributed equally to this work. X.L. and M.Q. proposed the idea and designed the experiment. M.Q. fabricated and characterized perovskite solar cells. Y.L. synthesized perovskite quantum dots with the assistance of S.L. M.Q. conducted XRD and GIWAXS measurements with the assistance of P.F.C. and Z.Q. C.-J.S. and Y.Y. conducted in situ GIWAXS measurements, and M.Q. analyzed the data. X.G. conducted cross-sectional TEM under

the supervision of Y.Z. L.S. conducted ToF-SIMS under the supervision of Z.F. M.Q., Y.L., and X.L. prepared the manuscript. All authors discussed the results and commented on the manuscript.

### Notes

The authors declare no competing financial interest.

### ACKNOWLEDGMENTS

We are grateful for the beam time and technical support provided at 23A SWAXS beamline and BL09A2 U5 beamline at the National Synchrotron Radiation Research Center (NSRRC), Hsinchu and beamline BL17B1 in Shanghai Synchrotron Radiation Facility (SSRF). X.L. acknowledges financial support from the National Natural Science Foundation of China (No. 52122004), Research Grant Council (RGC) of Hong Kong (No. 14305721), and CUHK PIEF and CRIMS Grant (No. 3133288). Y.Z. thanks the Hong Kong RGC (No. 15305020) and Hong Kong Polytechnic University (No. ZVRP) for financial support.

### REFERENCES

- (1) Miyasaka, T.; Kulkarni, A.; Kim, G. M.; Öz, S.; Jena, A. K. Perovskite Solar Cells: Can We Go Organic-Free, Lead-Free, and Dopant-Free? *Adv. Energy Mater.* **2020**, *10* (13), 1902500.
- (2) Gu, S.; Lin, R.; Han, Q.; Gao, Y.; Tan, H.; Zhu, J. Tin and Mixed Lead–Tin Halide Perovskite Solar Cells: Progress and their Application in Tandem Solar Cells. *Adv. Mater.* **2020**, *32* (27), 1907392.
- (3) Cao, J.; Yan, F. Recent Progress of Tin-based Perovskite Solar Cells. *Energy Environ. Sci.* **2021**, *14* (3), 1286–1325.
- (4) Shockley, W.; Queisser, H. J. Detailed Balance Limit of Efficiency of p-n Junction Solar Cells. *J. Appl. Phys.* **1961**, *32* (3), 510–519.
- (5) Wang, C.; Zhang, Y.; Gu, F.; Zhao, Z.; Li, H.; Jiang, H.; Bian, Z.; Liu, Z. Illumination Durability and High-Efficiency Sn-Based Perovskite Solar Cell under Coordinated Control of Phenylhydrazine and Halogen Ions. *Matter* **2021**, *4* (2), 709–721.
- (6) Abdel-Shakour, M.; Chowdhury, T. H.; Matsushita, K.; Bedja, I.; Moritomo, Y.; Islam, A. High-Efficiency Tin Halide Perovskite Solar Cells: The Chemistry of Tin (II) Compounds and Their Interaction with Lewis Base Additives during Perovskite Film Formation. *Solar RRL* **2021**, *5* (1), 2000606.
- (7) Jiang, X.; Zang, Z.; Zhou, Y.; Li, H.; Wei, Q.; Ning, Z. Tin Halide Perovskite Solar Cells: An Emerging Thin-Film Photovoltaic Technology. *Acc. Mater. Res.* **2021**, *2* (4), 210–219.
- (8) Chen, Q.; Bai, L.; Tsiba Matondo, J.; Deng, M.; Malouangou Maurice, D.; Gul, M. Additive Engineering for Sn-Based PSCs: Enhancement of Open-Circuit Voltage and Fill Factor. *Sol. Energy* **2021**, *214*, 26–50.
- (9) Ke, W.; Stoumpos, C. C.; Kanatzidis, M. G. Unleaded<sup>†</sup> Perovskites: Status Quo and Future Prospects of Tin-Based Perovskite Solar Cells. *Adv. Mater.* **2019**, *31* (47), 1803230.
- (10) Jokar, E.; Chien, C.-H.; Fathi, A.; Rameez, M.; Chang, Y.-H.; Diao, E. W.-G. Slow Surface Passivation and Crystal Relaxation with Additives to Improve Device Performance and Durability for Tin-Based Perovskite Solar Cells. *Energy Environ. Sci.* **2018**, *11* (9), 2353–2362.
- (11) Li, G.; Su, Z.; Li, M.; Yang, F.; Aldamasy, M. H.; Pascual, J.; Yang, F.; Liu, H.; Zuo, W.; Di Girolamo, D.; Iqbal, Z.; Nasti, G.; Dallmann, A.; Gao, X.; Wang, Z.; Saliba, M.; Abate, A. Ionic Liquid Stabilizing High-Efficiency Tin Halide Perovskite Solar Cells. *Adv. Energy Mater.* **2021**, *11* (32), 2101539.
- (12) Li, M.; Zuo, W.-W.; Yang, Y.-G.; Aldamasy, M. H.; Wang, Q.; Cruz, S. H. T.; Feng, S.-L.; Saliba, M.; Wang, Z.-K.; Abate, A. Tin Halide Perovskite Films Made of Highly Oriented 2D Crystals Enable More Efficient and Stable Lead-free Perovskite Solar Cells. *ACS Energy Lett.* **2020**, *5* (6), 1923–1929.
- (13) Kovaricek, P.; Nadazdy, P.; Pluharova, E.; Brunova, A.; Subair, R.; Vegso, K.; Guerra, V. L. P.; Volochanskyi, O.; Kalbac, M.; Krasnansky, A.; Pandit, P.; Roth, S. V.; Hinderhofer, A.; Majkova, E.; Jergel, M.; Tian, J.; Schreiber, F.; Siffalovic, P. Crystallization of 2D Hybrid Organic–Inorganic Perovskites Templated by Conductive Substrates. *Adv. Funct. Mater.* **2021**, *31* (13), 2009007.
- (14) Bi, D.; Yi, C.; Luo, J.; Décoppet, J.-D.; Zhang, F.; Zakeeruddin, S. M.; Li, X.; Hagfeldt, A.; Grätzel, M. Polymer-Templated Nucleation and Crystal Growth of Perovskite Films for Solar Cells with Efficiency Greater Than 21%. *Nat. Energy* **2016**, *1* (10), 16142.
- (15) Zhang, H.; Qin, M.; Chen, Z.; Yu, W.; Ren, Z.; Liu, K.; Huang, J.; Zhang, Y.; Liang, Q.; Chandran, H. T.; Fong, P. W. K.; Zheng, Z.; Lu, X.; Li, G. Bottom-Up Quasi-Epitaxial Growth of Hybrid Perovskite from Solution Process—Achieving High-Efficiency Solar Cells via Template-Guided Crystallization. *Adv. Mater.* **2021**, *33* (22), 2100009.
- (16) Moloney, E. G.; Yeddu, V.; Saidaminov, M. I. Strain Engineering in Halide Perovskites. *ACS Mater. Lett.* **2020**, *2* (11), 1495–1508.
- (17) Gu, Z.; Zhou, Z.; Huang, Z.; Wang, K.; Cai, Z.; Hu, X.; Li, L.; Li, M.; Zhao, Y. S.; Song, Y. Controllable Growth of High-Quality Inorganic Perovskite Microplate Arrays for Functional Optoelectronics. *Adv. Mater.* **2020**, *32* (17), 1908006.
- (18) Swarnkar, A.; Marshall, A. R.; Sanehira, E. M.; Chernomordik, B. D.; Moore, D. T.; Christians, J. A.; Chakrabarti, T.; Luther, J. M. Quantum Dot–Induced Phase Stabilization of  $\alpha$ -CsPbI<sub>3</sub> Perovskite For High-Efficiency Photovoltaics. *Science* **2016**, *354* (6308), 92–95.
- (19) Hermans, J. J.; Hermans, P. H.; Vermaas, D.; Weidinger, A. Quantitative Evaluation of Orientation in Cellulose Fibres from the X-ray Fibre Diagram. *Recl. Trav. Chim. Pays-Bas* **1946**, *65* (6), 427–447.
- (20) Ogle, J.; Powell, D.; Amerling, E.; Smilgies, D.-M.; Whittaker-Brooks, L. Quantifying Multiple Crystallite Orientations and Crystal Heterogeneities in Complex Thin Film Materials. *CrystEngComm* **2019**, *21* (38), 5707–5720.
- (21) Long, M.; Zhang, T.; Chen, D.; Qin, M.; Chen, Z.; Gong, L.; Lu, X.; Xie, F.; Xie, W.; Chen, J.; Xu, J. Interlayer Interaction Enhancement in Ruddlesden–Popper Perovskite Solar Cells toward High Efficiency and Phase Stability. *ACS Energy Lett.* **2019**, *4*, 1025–1033.
- (22) Qin, M.; Chan, P. F.; Lu, X. A Systematic Review of Metal Halide Perovskite Crystallization and Film Formation Mechanism Unveiled by In Situ GIWAXS. *Adv. Mater.* **2021**, *33*, 2105290.
- (23) Wu, W.-R.; Su, C.-J.; Chuang, W.-T.; Huang, Y.-C.; Yang, P.-W.; Lin, P.-C.; Chen, C.-Y.; Yang, T.-Y.; Su, A.-C.; Wei, K.-H.; Liu, C.-M.; Jeng, U. S. Surface Layering and Supersaturation for Top-Down Nanostructural Development during Spin Coating of Polymer/Fullerene Thin Films. *Adv. Energy Mater.* **2017**, *7* (14), 1601842.
- (24) Qin, M.; Xue, H.; Zhang, H.; Hu, H.; Liu, K.; Li, Y.; Qin, Z.; Ma, J.; Zhu, H.; Yan, K.; Fang, G.; Li, G.; Jeng, U. S.; Brocks, G.; Tao, S.; Lu, X. Precise Control of Perovskite Crystallization Kinetics via Sequential A-Site Doping. *Adv. Mater.* **2020**, *32* (42), 2004630.
- (25) Qin, M.; Tse, K.; Lau, T. K.; Li, Y.; Su, C. J.; Yang, G.; Chen, J.; Zhu, J.; Jeng, U. S.; Li, G.; Chen, H.; Lu, X. Manipulating the Mixed-Perovskite Crystallization Pathway Unveiled by In Situ GIWAXS. *Adv. Mater.* **2019**, *31* (25), 1901284.
- (26) Dang, H. X.; Wang, K.; Ghasemi, M.; Tang, M. C.; De Bastiani, M.; Aydin, E.; Duzon, E.; Barrit, D.; Peng, J.; Smilgies, D. M.; De Wolf, S.; Amassian, A. Multi-cation Synergy Suppresses Phase Segregation in Mixed-Halide Perovskites. *Joule* **2019**, *3* (7), 1746–1764.
- (27) Shi, T.; Zhang, H.-S.; Meng, W.; Teng, Q.; Liu, M.; Yang, X.; Yan, Y.; Yip, H.-L.; Zhao, Y.-J. Effects of Organic Cations on the Defect Physics of Tin Halide Perovskites. *J. Mater. Chem. A* **2017**, *5* (29), 15124–15129.
- (28) Dong, J. J.; Shao, S. Y.; Kahmann, S.; Rommens, A. J.; Hermida-Merino, D.; ten Brink, G. H.; Loi, M. A.; Portale, G.

Mechanism of Crystal Formation in Ruddlesden-Popper Sn-Based Perovskites. *Adv. Funct. Mater.* **2020**, *30* (24), 2001294.

(29) Zhao, Z.; Gu, F.; Li, Y.; Sun, W.; Ye, S.; Rao, H.; Liu, Z.; Bian, Z.; Huang, C. Mixed-Organic-Cation Tin Iodide for Lead-Free Perovskite Solar Cells with an Efficiency of 8.12. *Adv. Sci.* **2017**, *4* (11), 1700204.

(30) Jia, D.; Chen, J.; Mei, X.; Fan, W.; Luo, S.; Yu, M.; Liu, J.; Zhang, X. Surface Matrix Curing of Inorganic CsPbI<sub>3</sub> Perovskite Quantum Dots for Solar Cells with Efficiency Over 16. *Energy Environ. Sci.* **2021**, *14* (8), 4599–4609.

(31) Hu, L.; Zhao, Q.; Huang, S.; Zheng, J.; Guan, X.; Patterson, R.; Kim, J.; Shi, L.; Lin, C.-H.; Lei, Q.; Chu, D.; Tao, W.; Cheong, S.; Tilley, R. D.; Ho-Baillie, A. W. Y.; Luther, J. M.; Yuan, J.; Wu, T. Flexible and Efficient Perovskite Quantum Dot Solar Cells via Hybrid Interfacial Architecture. *Nat. Commun.* **2021**, *12* (1), 466.

(32) Hou, Y.; Zhou, Z. R.; Wen, T. Y.; Qiao, H. W.; Lin, Z. Q.; Ge, B.; Yang, H. G. Enhanced Moisture Stability of Metal Halide Perovskite Solar Cells Based on Sulfur–Oleylamine Surface Modification. *Nanoscale Horiz* **2019**, *4* (1), 208–213.

(33) Lee, J.-W.; Tan, S.; Han, T.-H.; Wang, R.; Zhang, L.; Park, C.; Yoon, M.; Choi, C.; Xu, M.; Liao, M. E.; Lee, S.-J.; Nuryyeva, S.; Zhu, C.; Huynh, K.; Goorsky, M. S.; Huang, Y.; Pan, X.; Yang, Y. Solid-Phase Hetero Epitaxial Growth of  $\alpha$ -Phase Formamidinium Perovskite. *Nat. Commun.* **2020**, *11* (1), 5514.

(34) Kim, H.-S.; Park, N.-G. Importance of Tailoring Lattice Strain in Halide Perovskite Crystals. *npj Asia Mater.* **2020**, *12* (1), 78.

(35) Williamson, G. K.; Hall, W. H. X-ray Line Broadening from Filled Aluminium and Wolfram. *Acta Metall.* **1953**, *1* (1), 22–31.

(36) Nishimura, K.; Hirotsu, D.; Kamarudin, M. A.; Shen, Q.; Toyoda, T.; Ikubo, S.; Minemoto, T.; Yoshino, K.; Hayase, S. Relationship between Lattice Strain and Efficiency for Sn-Perovskite Solar Cells. *ACS Appl. Mater. Interfaces* **2019**, *11* (34), 31105–31110.

(37) Jones, T. W.; Oshero, A.; Alsari, M.; Sponseller, M.; Duck, B. C.; Jung, Y.-K.; Settens, C.; Niroui, F.; Brenes, R.; Stan, C. V.; Li, Y.; Abdi-Jalebi, M.; Tamura, N.; Macdonald, J. E.; Burghammer, M.; Friend, R. H.; Bulović, V.; Walsh, A.; Wilson, G. J.; Lilliu, S.; Stranks, S. D. Lattice Strain Causes Non-Radiative Losses in Halide Perovskites. *Energy Environ. Sci.* **2019**, *12* (2), 596–606.

(38) Li, M.; Li, F.; Gong, J.; Zhang, T.; Gao, F.; Zhang, W.-H.; Liu, M. Advances in Tin(II)-Based Perovskite Solar Cells: From Material Physics to Device Performance. *Small Struct* **2022**, *3* (1), 2100102.

(39) Ji, L.; Zhang, T.; Wang, Y.; Liu, D.; Chen, H.; Zheng, H.; Peng, X.; Yuan, S.; Chen, Z. D.; Li, S. Regulating Crystallization Dynamics and Crystal Orientation of Methylammonium Tin Iodide Enables High-Efficiency Lead-Free Perovskite Solar Cells. *Nanoscale* **2022**, *14* (4), 1219–1225.

(40) Ke, W.; Stoumpos, C. C.; Spanopoulos, I.; Mao, L.; Chen, M.; Wasielewski, M. R.; Kanatzidis, M. G. Efficient Lead-Free Solar Cells Based on Hollow {en}MASnI<sub>3</sub> Perovskites. *J. Am. Chem. Soc.* **2017**, *139* (41), 14800–14806.

(41) Choi, W.-G.; Park, C.-G.; Kim, Y.; Moon, T. Sn Perovskite Solar Cells via 2D/3D Bilayer Formation through a Sequential Vapor Process. *ACS Energy Lett.* **2020**, *5* (11), 3461–3467.

(42) Lanzetta, L.; Webb, T.; Zibouche, N.; Liang, X.; Ding, D.; Min, G.; Westbrook, R. J. E.; Gaggio, B.; Macdonald, T. J.; Islam, M. S.; Haque, S. A. Degradation Mechanism of Hybrid Tin-Based Perovskite Solar Cells and the Critical Role of Tin (IV) Iodide. *Nat. Commun.* **2021**, *12* (1), 2853.

(43) Cao, J.; Yan, F. Recent Progress in Tin-Based Perovskite Solar Cells. *Energy Environ. Sci.* **2021**, *14* (3), 1286–1325.

(44) Wang, P.; Xie, J.; Xiao, K.; Hu, H.; Cui, C.; Qiang, Y.; Lin, P.; Arivazhagan, V.; Xu, L.; Yang, Z.; Yao, Y.; Lu, T.; Wang, Z.; Yu, X.; Yang, D. CH<sub>3</sub>NH<sub>3</sub>PbBr<sub>3</sub> Quantum Dot-Induced Nucleation for High Performance Perovskite Light-Emitting Solar Cells. *ACS Appl. Mater. Interfaces* **2018**, *10* (26), 22320–22328.

(45) Liu, Y.; Dong, Y.; Zhu, T.; Ma, D.; Proppe, A.; Chen, B.; Zheng, C.; Hou, Y.; Lee, S.; Sun, B.; Jung, E. H.; Yuan, F.; Wang, Y.-k.; Sagar, L. K.; Hoogland, S.; García de Arquer, F. P.; Choi, M.-J.; Singh, K.; Kelley, S. O.; Voznyy, O.; Lu, Z.-H.; Sargent, E. H. Bright

and Stable Light-Emitting Diodes Based on Perovskite Quantum Dots in Perovskite Matrix. *J. Am. Chem. Soc.* **2021**, *143* (38), 15606–15615.

(46) Xie, L.; Vashishtha, P.; Koh, T. M.; Harikesh, P. C.; Jamaludin, N. F.; Bruno, A.; Hooper, T. J. N.; Li, J.; Ng, Y. F.; Mhaisalkar, S. G.; Mathews, N. Realizing Reduced Imperfections via Quantum Dots Interdiffusion in High Efficiency Perovskite Solar Cells. *Adv. Mater.* **2020**, *32* (40), 2003296.

(47) Zhang, J.; Wang, L.; Jiang, C.; Cheng, B.; Chen, T.; Yu, J. CsPbBr<sub>3</sub> Nanocrystal Induced Bilateral Interface Modification for Efficient Planar Perovskite Solar Cells. *Adv. Sci.* **2021**, *8* (21), 2102648.